Available online at www.sciencedirect.com

ScienceDirect

journal homepage: www.elsevier.com/locate/he

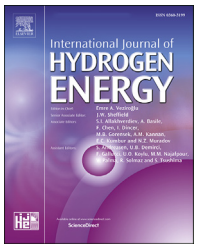

Cost-effective ion-tuning of Birnessite structures for efficient ORR electrocatalysts

Altantuya Ochirkhuyag [a], *Tamás Varga* [a], *Ildikó Y. Tóth* [a], *Ágnes Tímea Varga* [a], *András Sápi* [a,*], *Ákos Kukovecz* [a], *Zoltán Kónya* [a,b]

[a] *University of Szeged, Interdisciplinary Excellence Centre, Department of Applied and Environmental Chemistry, H-6720, Rerrich Béla Tér 1, Szeged, Hungary*

[b] *MTA-SZTE Reaction Kinetics and Surface Chemistry Research Group, University of Szeged, H-6720, Rerrich Béla Tér 1, Szeged, Hungary*

HIGHLIGHTS

- K-, Cu-Birnessite nanostructures by cheap oone pot method for ORR.
- Birnessite showed high activity in ORR with the 4-electron pathway.
- Cu effecting the Mn^{3+}/Mn^{4+} ratio resulting in good ORR activity.

ARTICLE INFO

Article history:
Received 8 January 2020
Received in revised form
2 April 2020
Accepted 6 April 2020
Available online 16 May 2020

Keywords:
Birnessite
Interlayer cation
Electrochemistry
Catalyst
ORR

ABSTRACT

Birnessite structured MnO_x with tuned potassium, copper and water content in the interlayer spacing is produced by a simple and cost-effective method. The new structures are investigated by XRD, Raman spectroscopy, SEM, EDX, HRTEM, DLS, TG, and DSC. Our study demonstrates a successful intercalation process to produce birnessites with mixed interlayer cations. Both Birnessite and Cu^{2+}/Birnessite structure have a nanosheet-like morphology where the sizes of the copper-treated birnessite nanoparticles are drastically decreased compared to the copper ion free structures. The specific surface area is increased from 21.6 m^2/g to 77.8 m^2/g in the presence of copper as a result of a longer ageing process. Our study reveals that the electron transfer numbers of Birnessite and Cu^{2+}/Birnessite are about 3.40 and 3.65, respectively in the oxygen reduction reaction. Both as-synthesized pristine Birnessite and copper tuned Birnessite are a promising candidate for a cheap, noble metal-free electrocatalyst for fuel cell applications.

Introduction

The world's most pressing concerns today are the future exhaust of conventional energy reserves [1] and the increasing environmental pollution from the byproduct of these sources, such as greenhouse gas emission from fossil fuel combustion [2]. Researchers are focusing to find sustainable energy resources and to provide ecologically friendly and cost-effective technologies and processes for further energy production. The energy conversion from renewable sources sharply increased in the last several decades using various advanced processes

* *Corresponding author.*
E-mail address: sapia@chem.u-szeged.hu (A. Sápi).

https://doi.org/10.1016/j.ijhydene.2020.04.022

such as the electrochemical fuel cell technology including two key steps: hydrogen oxidation reaction (HOR) [3], and oxygen reduction reaction (ORR) [4]. The electrochemical energy conversion in a fuel cell is a promising candidate for sustainable energy production [5,6] due to a wide range of application, and high energy efficiency [7,8]. Most of the energy conversion processes including ORR have slow reaction kinetics [9], which can be boosted by catalysts. Noble metal-based catalysts are one of the most common heterogeneous catalysts for ORR such as Pt–M_2O_3/C (M = Y or Gd) [10], Pd-RuSe/C [11], and Pt/CeO_2/C [12], but their relative rarity and high cost is making them unpractical. Therefore, electrochemical ORR catalyst research is focusing more on earth-abundant and cost-effective noble-metal free materials such as ZIF-67-derived CoO [13], iron nitride/nitrogen-doped graphene [14], nitrogen-doped carbon nanofiber [15], copper/graphite oxide [16], and $NiCo_2O_4$ [17].

Since the manganese is the second most abundant transition metal in the earth's crust, manganese oxide-based materials are increasingly studied as the ORR catalyst, for instance, MnO_x [18,19], Ag/MnO_x [20], NiOx-MnOx-graphene [21], Mn_3O_4 decorated *N*-doped carbon [22], and porous Mn_2O_3 [23]. However, manganese oxides have numerous different crystal structures even if they have the same number of oxidation state, for example, manganese (IV) oxide has several polymorphs: α-MnO_2, γ-MnO_2, δ-MnO_2, and λ-MnO_2. From these polymorphs, Delta(δ)-manganese oxide, also known as birnessite, is one of the most common manganese minerals in nature, which was first described in 1956 [24], and it has the following constitution: $(Na_{0.3}Ca_{0.1}K_{0.1})(Mn^{4+}, Mn^{3+})_2O_4 \cdot 1.5\,H_2O$). As a consequence of layered structure and earth-abundance, an increasing number of studies have investigated birnessite as a water oxidation catalyst [25] and as a supercapacitor [26]; but, only limited research was done on birnessite as an efficient cathode catalyst for the oxygen reduction reaction [27,28] Recently, one study revealed that birnessite type oxide has higher ORR catalytic activity than other polymorphs [29]. Interlayer molecules such as water, and cations (K^+, Na^+, Ca^{2+}, Mg^{2+}) are playing an essential role in electrochemical property of birnessite. Numerous studies have reported the effect of the interlayer cation exchanges, and the number of water molecules on the catalytic activity such as for water oxidation [30] and oxygen evaluation reaction [31]. According to literature, copper doping is enhancing the catalytic activity of other types of manganese oxide-based catalysts in ORR such as $Cu_xMn_{3-x}O_4$ spinel particles/polypyrrol composite [32], graphene-Cu-α-MnO_2 nanowire blends [33,34], and PtNiCu [35]. Despite these results, no research was done up until now on copper doped delta-manganese oxide catalyzed ORR processes.

Our goal was not only to investigate copper doping influence on the catalytic activity of birnessite but also to find a reliable method to synthesize birnessite. Birnessite contains Mn^{3+} and Mn^{4+} ions, where Mn^{3+} can be reduced to Mn^{2+}, or oxidized into Mn^{4+}, and M^{4+} can be reduced to Mn^{3+} and Mn^{2+}. This alternation of oxidation state particularly Mn^{3+} species increases catalysis of the ORR process [36], but it is challenging to control phase changes, and oxidation state ratios of the birnessite, which has been an essential part of the production and application. On account of this problem, a typical synthesis of birnessite requires hydrothermal condition, constant cooling, organic template, and the conventional reflux synthetic method [37].

In this report, we produced birnessite with a cost-effective and straightforward method described by Boumaiza et al. [38]. Modified by tuning the ageing time, which affects the amount of exchange from potassium (K^+) cation to copper (Cu^{2+})-ions as well as the concentration of the water in the interlayer space of the structure. The characterization of the as-synthesized material was done and the activity for oxygen reduction reaction was investigated with voltammetry and chronoamperometric methods. The study revealed that copper ion tuning is changing the Mn^{3+}/Mn^{4+} ratio and longer ageing process is increasing surface area and decreasing particle size, those are providing more active sites for the contact between catalyst and electrolyte.

Materials and methods

Chemicals

Manganese(II)-chloride-tetrahydrate ($MnCl_2$*$4H_2O$), potassium-permanganate ($KMnO_4$), copper(II)-chloride ($CuCl_2$) and potassium hydroxide (KOH) were purchased from Sigma Aldrich. All chemicals and reagents used in this study were at least in analytical grade and used without further purification. Ultrapure water was used for all synthesis.

Synthesis of Birnessite

Three aqueous solutions were used for the synthesis of potassium-birnessite: 1.75 ml of KOH (8.8 mol L^{-1}), 2.125 ml $KMnO_4$ (0.1 mol L^{-1}) and 3.75 ml $MnCl_2$ (0.6 mol L^{-1}). The synthesis method [38] used in the present work consisted of mixing ($MnCl_2$) and $KMnO_4$ solutions under vigorous stirring for 2 h then KOH-solution was dropwise added into this mixture. The final reaction mixture was then stirred for another 30 min and aged at 60 °C for 16 h. The final product was centrifuged and washed until the pH of the solution settled between 8 and 9 and dried at 60 °C overnight. Synthesis scheme showed in Supplementary material (Fig. S1). For the Cu^{2+}/Birnessite structure, $MnCl_2$ (0.5 mol L^{-1}) and $KMnO_4$ (0.1 mol L^{-1}) mixed with $CuCl_2$ (0.1 mol L^{-1}) for 2 h then KOH (8.8 mol L^{-1}) solution was added dropwise into this mixture. The final reaction mixture was then stirred for another 30 min and aged at 60 °C for 48 h. The intercalated birnessite was finally centrifuged and washed until the pH of the solution settled between 8 and 9 and dried at 60 °C overnight.

Basic characterization of the Birnessite structures

The intercalation of Birnessite samples was investigated by X-ray diffractometer (XRD) and Raman spectroscopy. The morphology was studied by scanning electron microscopy (SEM) and transmission electron microscopy (TEM), the chemical composition was calculated from energy-dispersive X-ray spectroscopy (EDS). The specific surface area and pore diameter were measured by nitrogen adsorption, while the thermal properties were investigated using thermogravimetry

(TG) and differential scanning calorimetry (DSC). The pH-dependent surface charge and aggregation state were studied by zeta potential measurement, and by dynamic light scattering (DLS). The detailed description of these techniques and methods are given in the supplementary information.

Electrochemical (ORR) measurements

The ORR electrode is prepared by the modification of a glassy carbon electrode with a mixture of the birnessite sample and carbon black slurry. The ORR measurements were performed in a three-electrode cell using the electrochemical workstation. The ORR preparation and measurements are detailed in the supplementary material.

Result and discussion

Structural determination and chemical characterization

XRD patterns of the potassium birnessite (Birnessite) and copper intercalated one (Cu^{2+}/Birnessite) are shown in Fig. 1a. The two main reflection peaks observed at 12.63° (dspacing = 0.69 nm calculated from Bragg's equation [39]) and 24.8° (dspacing = 0.36 nm) correspond to the (001) and (002) crystal planes of Birnessite, respectively [38,40]. The addition of the copper-ions resulted in a slight shift of (001) reflection from 12.81° (dspacing = 0.69 nm) to 12.63° (dspacing = 0.70 nm) (Fig. 1b.). The interlayer distance expansion can be attributed to the bigger size of the copper-ions as well as the higher amount of total interlayer cations [41] in Fig. 1(c-d). In the case of the pristine Birnessite, the reflection at 27.0° (dspacing = 0.32 nm) corresponds to the impurity raised from manganite (MnO(OH)) which is an intermediate phase during the birnessite formation. However, this phase is not observable for the copper intercalated birnessite structure. A weak reflection at ~19° and ~35° appears, which refers to the presence of a small amount of the tunnel structured(α-MnO_2) cryptomelane [42] as a result of a longer ageing process. Only complete phase changes observed in XRD (Fig. S2) after thermal gravimetric analysis where samples heated up until 750 °C.

Raman spectra of the samples are shown in Fig. 2a. The major peak at 582 cm^{-1} corresponds to the ν_3 (Mn–O) stretching vibration in the basal plane of the MnO_6 sheets [43], which is slightly shifted in case of Cu^{2+}/Birnessite to 580 cm^{-1}. It correlates with interlayer distance changes as observed in XRD results (Fig. 1b.). Further six peaks at 285, 411, 478, 513 and 640 cm^{-1} can be obtained for both samples which are correlating well with typical Raman shifts of birnessite in the literature [44]. Notably, a copper cation being present in the interlayer structure of Cu^{2+}/Birnessite, the intensity of the peak positioned at 565 cm^{-1} is significantly decreased [30,45]. Besides, in case of the Cu^{2+}-ion intercalated birnessite, a peak observed at 697 cm^{-1} (out-of-plane symmetric stretching of Mn–O of MnO_6) groups are attributing to changes of Mn^{4+}/Mn^{3+} ratio in the birnessite structure and disordering of the octahedral sheets when Cu^{2+}-ion are integrated into the interlayer space and illustration of the cryptomelane structure forming [46].

Energy-dispersive X-ray spectra of birnessite showed in Fig. 2b. The atomic percentage of oxygen is about 73–75 at%, manganese content around 18 at% and the interlayer cationic content (including potassium for Birnessite and copper/potassium for Cu^{2+}/Birnessite) is about 3–7 at% for both samples, which is similar to typical birnessites [47]. The calculated formula is $K_{0.18}MnO_2{*}xH_2O$ for Birnessite sample, and $Cu_{0.20}K_{0.15}MnO_2{*}xH_2O$ for Cu^{2+}/Birnessite sample,

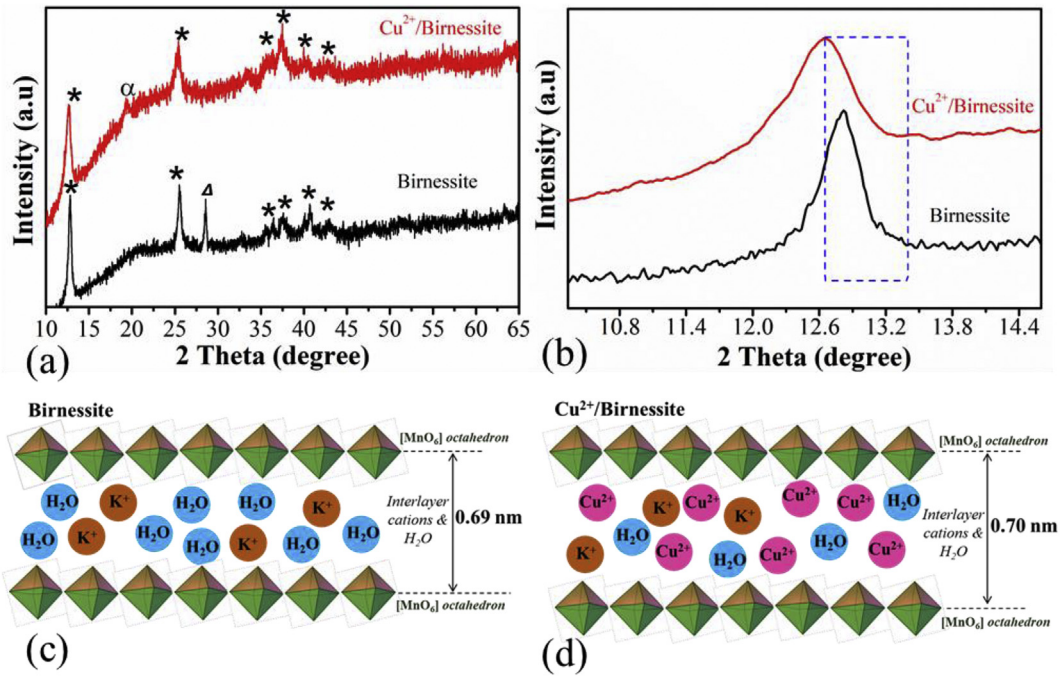

Fig. 1 – XRD patterns (a-b) {XRD patterns: * -birnessite, α-tunnel structured (MnO_2), Δ- manganite MnO(OH)} and Interlayer distance and intercalated cations of the Birnessite(c) and Cu^{2+}/Birnessite(d).

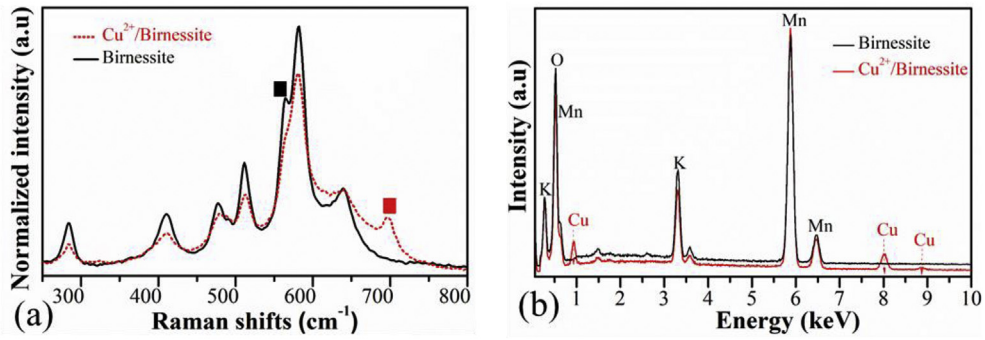

Fig. 2 – Raman spectra (a) Birnessite ■ 565 cm^{-1}(in-plane stretch) ■ 697 cm^{-1} (out-of-plane stretch), and EDX spectra (b) of the pristine birnessite as well as the copper-ion intercalated birnessite structure.

respectively [48] based on molar ratio detected from the quantitative analysis showed in Table S1.

Thermal analysis of the samples at RT-750 °C in both air and nitrogen atmosphere with a heating rate of 5 °C/min are depicted in Fig. 3a. Thermal stability of birnessite increased significantly due to the longer ageing time and the decreasing of the interlayer water molecule and the insertion of copper cations into the interlayer. The first massive decomposition appears at ~120 °C with a mass loss of 10% and 6% for Birnessite and Cu^{2+}/Birnessite, respectively. These phenomena can be attributed to the desorption of physisorbed water and the removal of interlayer water [49]. The second decomposition occurs in 2–3 steps at 120–550 °C with a weight loss of 8% for Birnessite and 2% for Cu^{2+}/Birnessite, which can be attributed to the loss of lattice oxygen species. Slight weight increment of ~1% occurred at about 500 °C for the Cu^{2+}/Birnessite corresponding to the oxidation of manganese. In the literature, weakly crystallized synthetic birnessite shows similarly slight weight gain at 500–600 °C in the thermogravimetric analysis [50]. Thermal stability of both Birnessite sample is quite high, and only 8–18% of the total weight is lost before reaching 750 °C. For the understanding slight weight increment in the case of Cu^{2+}/Birnessite at elevated temperature, TG analysis was performed in a nitrogen atmosphere, too (Fig. S3). During the inert condition, no weight gain has appeared. In the case of the air-based measurements, the Cu^{2+}/Birnessite shows the presence of manganese oxidation of Mn^{3+} to Mn^{4+}, which is attributed to the increased amount of the Mn^{3+} and decreases of the amount of crystallization in the samples.

Differential Scanning Calorimetric results are shown in Fig. 3b. Endothermic peaks around 100 °C and 150–350 °C refer to the dehydration of the physical and the chemically adsorbed water molecules respectively, located between layers. In

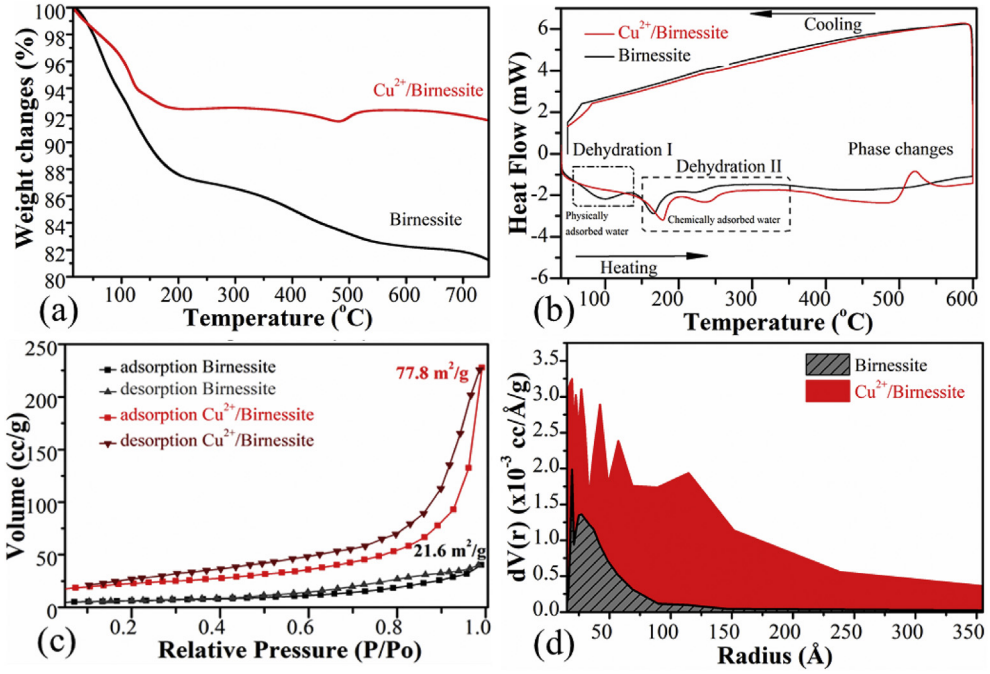

Fig. 3 – Thermal decomposition of the Birnessites and Cu^{2+}/Birnessite samples in the air (a). Differential scanning calorimetric analysis results (b), and N_2 adsorption-desorption isotherms (c), and pore diameter of the Birnessite samples (d).

the case of Cu^{2+}/Birnessite, an exothermic peak around 500 °C was observed which corresponds to the transformation of the layered structure to the tunnel structured cryptomelane due to the oxidation of Mn (III) to Mn (IV) [51,52].

N2 adsorption isotherms and pore diameter of the samples showed in Fig. 3c and d. Type IV N_2 adsorption isotherm was observable in the case of both samples. Birnessite displays a smaller specific surface area of 21.6 m^2/g as typical birnessites [49], while the specific surface area of Cu^{2+}/Birnessite was calculated to be 77.8 m^2/g, respectively in Fig. 3c. As can be seen in Fig. 3d, the pore diameter is 5 nm and 10–15 nm for Birnessite and Cu^{2+}/Birnessite, respectively showing that the copper ion modification resulted in a more mesoporous-like structure beside the increased surface area. The development of a more mesoporous-like structure for Birnessite and Cu^{2+}/Birnessite can be attributed to the doping of copper ion, which refines layered MnO_2 nanoparticles into tiny grains, while longer ageing process results in higher specific surface areas.

Morphological characterization

Scanning electron microscopic images showed that the birnessite consists of larger well-crystallized plates (sheet-like) with length from 100 nm to a few micrometres (Fig. 4a.). In the case of Cu^{2+}/Birnessite due to copper intercalation and longer ageing process, the sheets are smaller, and aggregated miniature sheets were formed with rod-like wires (Fig. 4b.). Transmission electron microscopic images of the samples (Fig. 4c and d) show similar morphological structures as images made by the SEM. HRTEM images (Fig. 4e and f.) reveal that the leading lattice distance of the Birnessite was 0.69 nm while it was measured to be 0.70 nm in case of Cu^{2+}/Birnessite pointing to the presence of a slight interlayer distance expansion due to the presence of Cu^{2+}-ions. These results correlate with results obtained by XRD (Fig. 1b.). Morphology of these samples is similar to the typical birnessite structures as published in the literature [53].

The pH-dependent aggregation state and zeta potential

In water-based systems, the metal oxide particles have variable surface charges. The most critical parameters of this phenomena are the pH [54] and ionic strengths [54,55]. The pH-dependent zeta potential (ζ) and hydrodynamic diameter (Z_{AVE}) of the original Birnessite particles, as well as the effect of Cu^{2+}-ion additions on the surface charges and the aggregation state of the birnessites, are shown in Fig. 4. The surfaces of the Birnessite particles become charged in water due to the reactions of their surface hydroxyl groups (≡Mn–OH), controlled by both the pH and the ionic strengths of the medium [56]. The protonation/deprotonation reactions of (≡Mn–OH) sites lead to the formation of positive ($\equiv Mn-OH_2^+$) or negative ($\equiv Mn-O^-$) surface charges. The pH is at pH~2.5 for Birnessite particles at the isoelectric point (I.E.P.), where $\zeta = 0$ mV, which is in good agreement with previously published measurement [56]. Around this pH value, the particles are aggregating (Z_{AVE} > 1000 nm) because of the lack of the electrostatic stabilization. Due to presence of ($\equiv Mn-O^-$) surface groups, colloidally stable dispersion can be observed at pH values between 4 and 10, accompanied by a low Z_{AVE} and high absolute value of ζ (see Fig. 5a.). The large amount of Na^+-ion (~100 mmol L^{-1}) added into the system as NaOH solution to set the pH around 13, which results in the so-called screen effect. The success of the dispersion process was confirmed by the ~200 nm measured Z_{AVE} value in the temporarily stable regime, which is very close to the lower value of the particle size determined by SEM.

The I.E.P. of Cu^{2+}/Birnessite is shifted from pH~2.5 to pH~3.5 (see Fig. 5b). The addition of Cu ions can lead to the number of chemical alterations in the mixture. First, the intercalated K ions can be exchanged by polyvalent Cu cations (justified by the lattice distance changes determined by XRD). The charge of cations can modulate the oxidative state of the manganese in the layer, namely, they are partially converted from the stable Mn^{4+} to Mn^{3+} (proved by Raman spectroscopy, TG, EDX). This phenomenon affects the surface charge properties due to the shift of the (≡Mn–OH) groups' pK. Secondly, a small part of the added Cu ions could form an oxide/hydroxide nanoparticle. These nanoparticles have own surface functional groups (≡S–OH) with representative protonation/deprotonation equilibrium. Based on the literature, the I.E.P. of copper-oxide nanoparticles is about pH~6.8 [57], so the contribution of the protonated ($\equiv Cu-OH_2^+$) surface groups (pH > I.E.P.) can explain the shift of the ζ values presented in Fig. 5b. Furthermore, these changes result in the increase of the aggregation regime for Cu^{2+}/Birnessite (see Fig. 4c) probably due to heterogeneous coagulation.

According to the ζ measurements, we could improve and prepare samples with the best parameters for the ORR investigations. As seen in ζ results, the Birnessite particles are aggregated in alkaline conditions, so the usage of carbon black during the preparation of the electrodes for ORR measurements is necessary to get an appropriate layer under the condition of ORR experiments.

Electrochemical characterization of ORR activity

ORR activity of the samples was examined using cyclic voltammetry and linear sweep voltammetry and their stability were tested by the chronoamperometric method. All electrochemical measurement was performed in alkaline media (0.1 M KOH) in a three-electrode glass cell, using glassy carbon electrode modified with the samples as the working electrode, Ag/AgCl electrode as reference electrode and platinum wire as a counter electrode.

As Fig. 6 shows, a reduction peak appears on the voltammograms measured in the oxygen-saturated electrolyte compared to the background measured in nitrogen saturated electrolyte. The peak position was 0.73 V vs RHE in case of pristine Birnessite (Fig. 6a) while it was 0.77 V vs RHE in case of the Cu^{2+}/Birnessite (Fig. 6b) modified GCE. The onset potential of the pristine Birnessite was measured to be 0.8 V vs RHE while this value was shifted in case of the Cu^{2+}/Birnessite modified GCE to 0.87 V vs RHE, similarly to the shift of the reduction peak position. These values are comparable to the results observed for common ORR catalysts [58]. Notably, the voltammograms in Fig. 6b show two oxidation peaks at 0.57 and 0.82 V vs RHE, which correspond to the oxidation peaks of Cu to Cu(I) and Cu(I) to Cu(II), respectively [16]. Elemental Cu can be originated from the reduction process of the Cu(II)

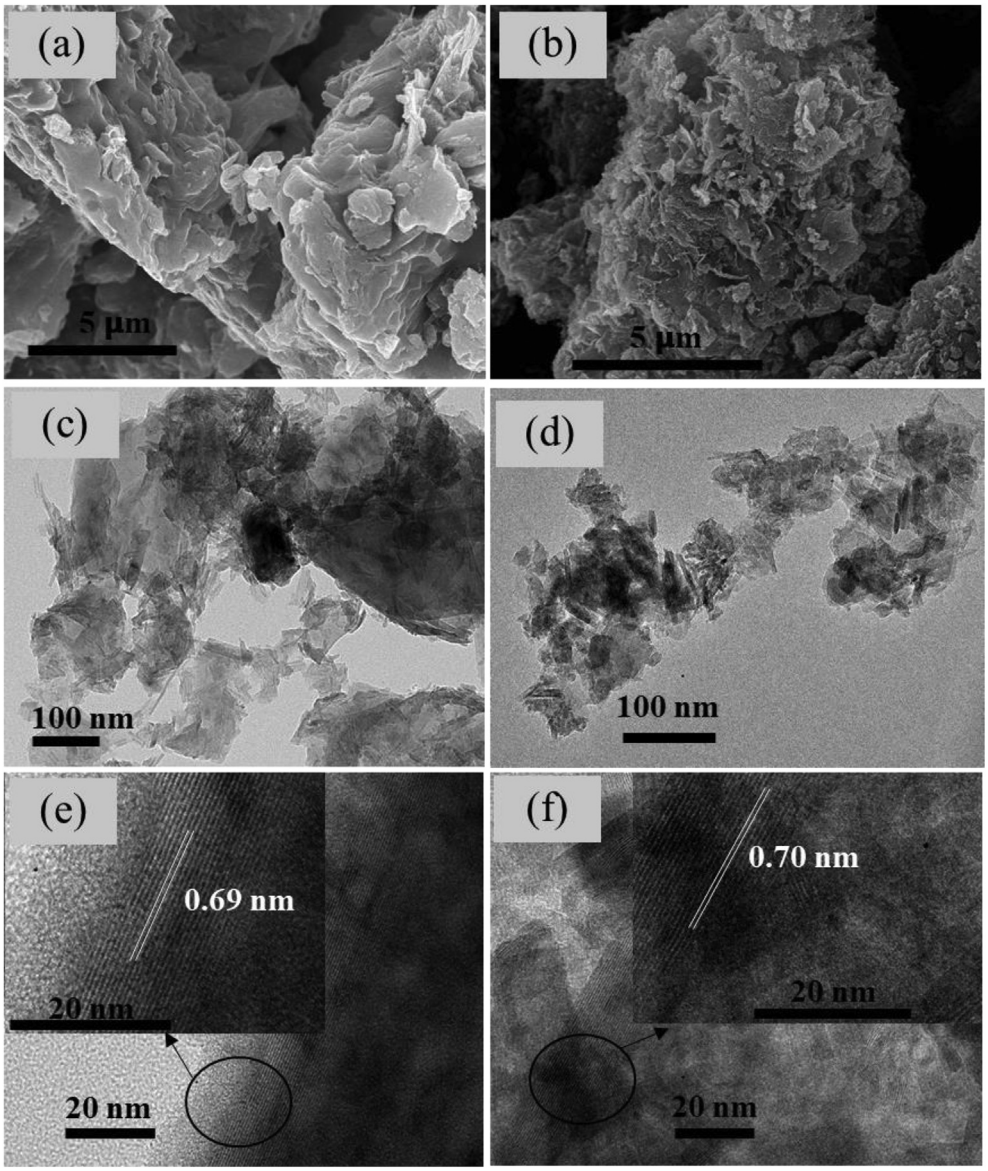

Fig. 4 – Typical SEM images (a-b) and TEM images (c-d), and HR-TEM images of the birnessite samples (e-f). The images created from undoped Birnessite samples on the left (a,c,e) and Cu^{2+}/Birnessite samples on the right (b,d,f).

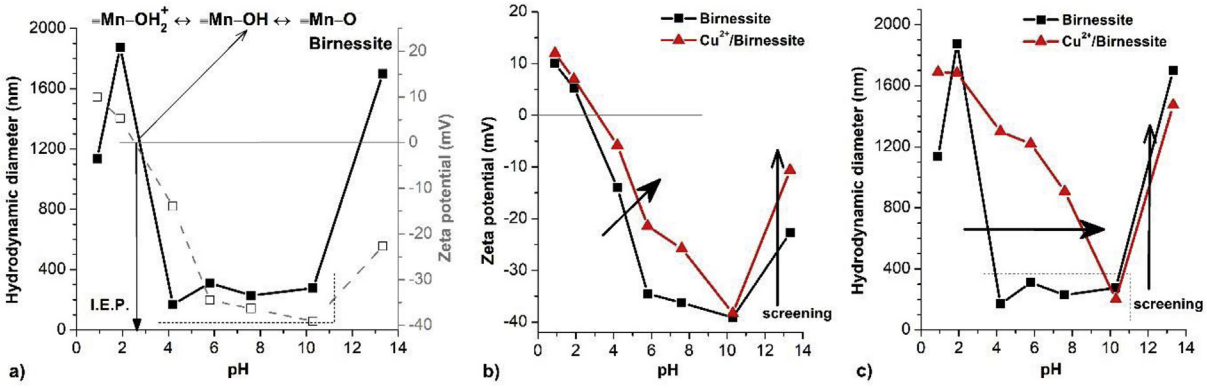

Fig. 5 – Characterization of the Birnessite (a) by the pH-dependent zeta potential (ζ) and hydrodynamic diameter (Z_{AVE}) at 10 mmol L^{-1} NaCl. Effect of Cu ion addition on (b) the zeta potential and (c) the hydrodynamic diameter of the Birnessites particles at 10 mmol L^{-1} NaCl.

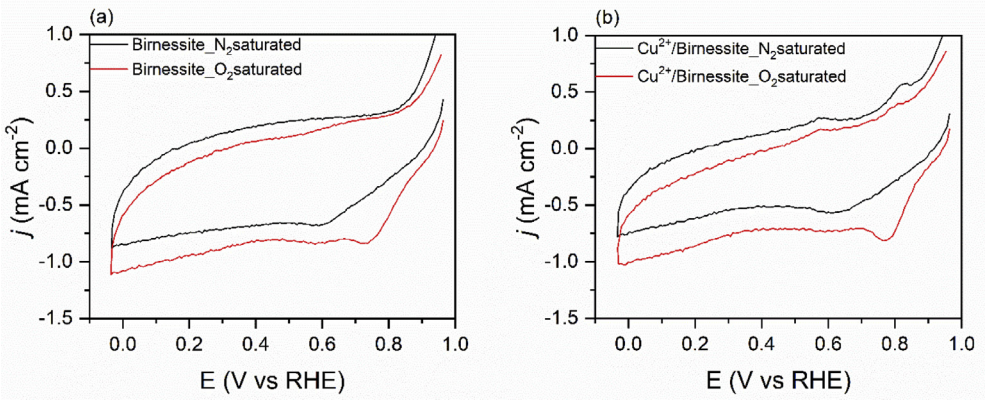

Fig. 6 – Cyclic voltammograms of the GCE electrodes modified with the as-prepared (a) Birnessite samples, and (b) Cu^{2+}/Birnessite samples. All measurements were carried out in 0.1 M KOH solution at 10 mVs^{-1} scan rates.

during the electrochemical measurement [59]. The reduction peaks are not visible on the measured voltammograms, likely because of the small amount of copper presented in the sample, which gives relatively small current values during the reduction process compared to that of the parallel oxygen reduction reaction [60].

Fig. 7a and b shows the LSV curves of the glassy carbon electrodes modified with the as-prepared samples. As it shows, the current density was increased with increasing rotation rates. Fig. 7c shows the comparison of the LSV curves at 1500 rpm rotation rate. The reduction peak shifted from 0.8 V to 0.87 V, although the reduction current densities (taken at 0 V vs RHE) did not change after the intercalation, which was measured to be 4.6 mA cm^{-2} for both pristine Birnessite and Cu^{2+}/Birnessite. Electron transfer numbers were calculated from the linear sweep voltammograms at different rotation rates by using the Koutecky Levich equation (for details see supplementary information) [61]. The Koutecky-Levich plot of the Birnessite-modified GCE electrodes at various potentials is depicted in Fig. S4. The parallel straight

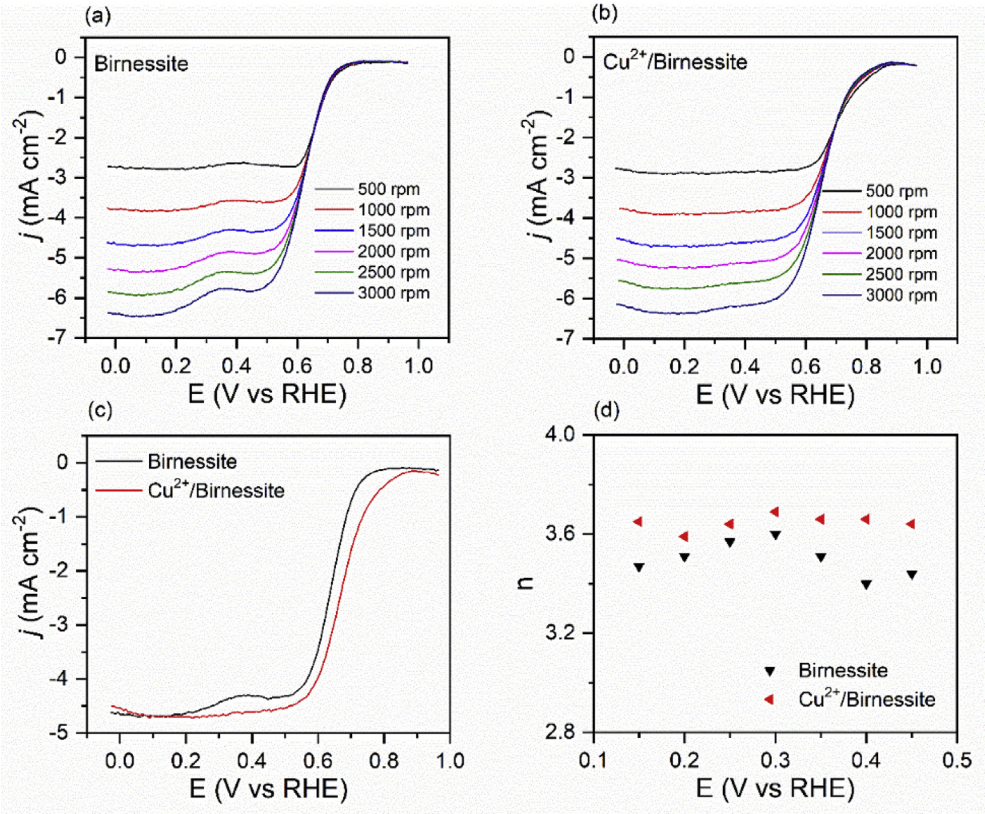

Fig. 7 – LSV curves of the GCE modified with (a) Birnessite and (b) Cu^{2+}/Birnessite. (d) LSV curves of the as-prepared sample measured at 1500 rpm. (d) Summary of the calculated electron transfer numbers. All measurements were carried out in 0.1 M KOH solution at 10 mVs^{-1} scan rates.

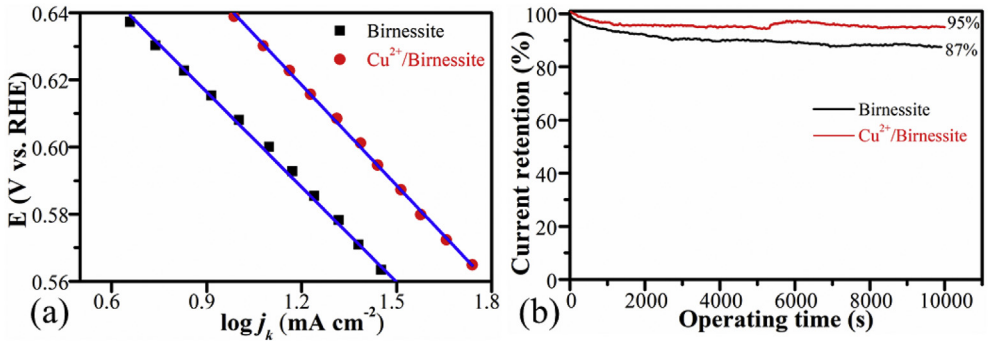

Fig. 8 – (a) Tafel slopes derived from LSV data and (b) Stability measurement of the samples measured at 0,4 V (vs RHE) in oxygen saturated electrolyte at 1500 rpm rotating rate. All measurements were carried out in 0.1 M KOH solution at 10 mVs^{-1} scan rates.

trend lines can be attributed to the first-order reaction kinetics of the ORR [62]. The extrapolated K-L plots have non-zero intercepts, thus mixed kinetic-diffusion control exists in the investigated potential range [63]. The calculated electron transfer numbers were summarized in Fig. 7d. It is seen, that the calculated electron transfer numbers are close to 4 (~3.4 and 3.6) in both Birnessite and Cu^{2+}/Birnessite case, and the oxygen reduction reaction mainly proceeds through the four-electron pathway with their use, proving that both samples show great promise as a cathode catalyst material for fuel cells.

The ORR activity was improved with Cu^{2+} ion-doped Birnessite catalyst compared to the activity with pristine Birnessite catalyst, based on the calculated ~10% electron transfer number increment, and the measured positive shift in the oxygen reduction potential peak and onset potential. These phenomena can be explained by several causes based on the literature. As others already stated, Mn^{3+}/Mn^{4+} oxidation state ratio plays an important role in ORR catalytic activity and ion-tuning (Ag^{+} and Zr^{4+}) increases Mn^{3+} ratio in birnessite type manganese oxides [28,64,65]. As shown in Raman spectra (Fig. 2a) the peak observed at 697 cm^{-1} corresponds to changes of Mn^{4+}/Mn^{3+} ratio in the birnessite structure and disordering of the octahedral sheets when Cu^{2+}-ion are integrated into the interlayer space [46]. Wang et al. found that the mutual action between the intercalated ion Zr^{4+} (in our case Cu^{2+}) and the Mn^{3+} ions results in increased O_2 adsorption for ORR [64]. A similar connection can be hypothesized between the birnessite and the intercalated copper ion, as Yaday et al. have already investigated the adsorption of oxygen species to the surface of similar material and found that the intercalated copper ion has beneficial effects on the birnessite type manganese-oxide [59]. Likewise, the smaller particle size is boosting the activity owing to the larger surface-to-bulk ratio and numerous surface defects. Higher surface areas provide more active sites for the contact between catalyst and electrolyte [66].

Fig. 8a shows the LSV derived Tafel slopes, where a slight increase can be experienced and the value was found to be −99,8 mV/dec for pristine Birnessite mv/dec and −94,4 for the Cu^{2+}/Birnessite. These values are also similar to those reported in the literature (ref: [20,28] from Table .1). The stability of the catalysts was evaluated by measuring the current retention-operating time curves with the chronoamperometric method at 0.4 V (vs RHE) potential in oxygen-saturated 0.1 M KOH solution at 1500 rpm rotating rate as seen in Fig. 8b. The stability study reveals that the as-synthesized birnessites have high stability with over 10,000 s operating time. It is exciting to note that Cu^{2+}/Birnessite shows higher stability (94.8% current retention) than pristine Birnessite sample (87.4% current retention), which can be the results of the interlayer copper ion stabilizing the Mn^{3+}/Mn^{4+} species in the catalyst during ORR [67]. As Yadav et al. explain, the reversibly intercalated copper stabilizes and enhances its charge transfer characteristics. As can be seen in Fig. 6b, a portion of copper ions can be reduced by oxygen and form an oxidized copper state, which is typical phenomena for the copper included ORR catalysts [16].

Table 1 – Manganese oxide-based ORR catalysts.

Catalyst	E_{onset} (V vs RHE)	$E_{1/2}$ (V vs RHE)	Tafel slope, mV	ETN (n)	Electrolyte solution	Stability test operation time (s), retention (%)	Reference
Birnessite	0.8	0.64	−99,8	3.4	0.1(M) KOH	10,000 s, 87%	This study
Cu^{2+}/Birnessite	0.87	0.67	−94,4	3.6	0.1(M) KOH	10,000 s, 95%	This study
Ag–MnO_2	0.83	-	89	4	0.1(M) KOH	45,000 s, 91%	[20]
Ag–MnO_2/C	0.87	0.80	−79	3.9	0.1(M) KOH	45,000 s, 97%	[28]
Cu-α-MnO_2	0.87	0.66	-	3.31	0.1(M) KOH	-	[34]
$NiMnO_2$-4.9	0.89	0.70	68	3.66	0.1(M) KOH	5000sec, >90%	[65]
Mn_3O_4/Nano-C	0.87	0.85	-	3.9	0.1(M) KOH	20,000 s, 97%	[68]
Mn_2O_3, MnO_2	0.4	-	-	4	0.1(M) KOH	-	[69]
MnO_x/C	-	-	50	2.4	0.1(M) KOH	-	[70]
MnOx-C(D)	-	-	-	3.81	0.1(M) KOH	-	[71]

The comparison of the ORR catalytic activity test results of the two synthesized samples with those of the literature can be seen in Table 1 The pristine birnessite and Cu^{2+}/birnessites samples both have the possibility to be utilized as a cathode catalyst in fuel cells as the results are comparable to other already published manganese oxide-based catalysts.

Conclusions

This work presented an alternate synthesis method for birnessite with different interlayered potassium and copper cations. The addition of copper and a longer ageing process resulted in a significant specific surface area increment (21.6 m^2/g to 77.8 m^2/g) as well as small nanoparticle-type morphology. It was also experimentally validated, that copper ion enhances the main active site Mn^{3+} in the birnessite structure, which results in an improved electron transfer number and higher stability during the ORR test. Significant four-electron transferability was observed for Cu^{2+}/Birnessite and for Birnessite at a smaller degree. Both catalysts proved to be highly stable with above 87–95% retention after 10,000-s measurement. These results prove that the synthesized Birnessite samples described in this paper, show great promise as an efficient, cheap, noble-metal-free electrochemical catalyst.

Acknowledgements

This paper was supported by the Hungarian Research Development and Innovation Office through grants NKFIH OTKA PD 120877 of AS. ÁK, and KZ is grateful for the fund of NKFIH (OTKA) K112531 & NN110676 and K120115, respectively. The financial support of the Hungarian National Research, Development and Innovation Office through the GINOP-2.3.2-15-2016-00013 project "Intelligent materials based on functional surfaces - from syntheses to applications" and the Ministry of Human Capacities through the EFOP-3.6.1-16-2016-00014 project and the 20391-3/2018/FEKUSTRAT are acknowledged. I.Y.T. also acknowledges the support by the Ministry of Human Capacities, Hungary through the grant "ÚNKP-19-4 New National Excellence Program".

Appendix ASupplementary data

Supplementary data to this article can be found online at https://doi.org/10.1016/j.ijhydene.2020.04.022.

REFERENCES

[1] Heinberg R, Fridley D. The end of cheap coal. Nature 2010;468:367–9. https://doi.org/10.1038/468367a.
[2] Perera F. Pollution from fossil-fuel combustion is the leading environmental threat to global pediatric health and equity: solutions exist. Int J Environ Res Publ Health 2018;15. https://doi.org/10.3390/ijerph15010016.
[3] Tzorbatzoglou F, Brouzgou A, Jing S, Wang Y, Song S, Tsiakaras P. Oxygen reduction and hydrogen oxidation reaction on novel carbon supported Pd_xIr_y electrocatalysts. Int J Hydrogen Energy 2018;43:11766–77. https://doi.org/10.1016/j.ijhydene.2018.02.071.
[4] Ma R, Lin G, Zhou Y, Liu Q, Zhang T, Shan G, Yang M, Wang J. A review of oxygen reduction mechanisms for metal-free carbon-based electrocatalysts. Npj Comput Mater. 2019;5. https://doi.org/10.1038/s41524-019-0210-3.
[5] Coralli A, Sarruf BJM, de Miranda PEV, Osmieri Luigi, Specchia S, Minh NQ. Chapter 2 - fuel cells. Elsevier Inc; 2019. https://doi.org/10.1016/B978-0-12-814251-6.00002-2.
[6] Das I, Noori MT, Bhowmick GD, Ghangrekar MM. Synthesis of bimetallic iron ferrite $Co0.5Zn0.5Fe_2O_4$ as a superior catalyst for oxygen reduction reaction to replace noble metal catalysts in microbial fuel cell. Int J Hydrogen Energy 2018;43:19196–205. https://doi.org/10.1016/j.ijhydene.2018.08.113.
[7] Mahapatra MK, Singh P. Fuel cells. Energy Conversion Technology; 2013. https://doi.org/10.1016/B978-0-08-099424-6.00024-7.
[8] Gonzalez ER, Srinivasan S. Electrochemistry of fuel cells for transportation applications. Int J Hydrogen Energy 1984;9:215–8. https://doi.org/10.1016/0360-3199(84)90121-6.
[9] Paridah M, Moradbak A, Mohamed A, abdulwahab taiwo Owolabi F, Asniza M, Abdul Khalid SH. We are IntechOpen, the world's leading publisher of Open Access books Built by scientists, for scientists TOP 1 %. 2016. p. 13. https://doi.org/10.5772/57353. Intech. i.
[10] Luo Y, Habrioux A, Calvillo L, Granozzi G, Alonso-Vante N. Thermally induced strains on the catalytic activity and stability of Pt-M_2O_3/C (M=Y or Gd) catalysts towards oxygen reduction reaction. ChemCatChem 2015;7:1573–82. https://doi.org/10.1002/cctc.201500130.
[11] Maheswari S, Sridhar P, Pitchumani S. Pd-RuSe/C as ORR specific catalyst in alkaline solution containing methanol. Fuel Cell 2012;12:963–70. https://doi.org/10.1002/fuce.201200069.
[12] Xu F, Wang D, Sa B, Yu Y, Mu S. One-pot synthesis of Pt/CeO_2/C catalyst for improving the ORR activity and durability of PEMFC. Int J Hydrogen Energy 2017;42:13011–9. https://doi.org/10.1016/j.ijhydene.2017.04.039.
[13] Yu Y, You S, Du J, Xing Z, Dai Y, Chen H, Cai Z, Ren N, Zou J. ZIF-67-derived CoO (tetrahedral Co_2+)@nitrogen-doped porous carbon protected by oxygen vacancies-enriched SnO_2 as highly active catalyst for oxygen reduction and Pt co-catalyst for methanol oxidation. Appl Catal B Environ 2019;259:118043. https://doi.org/10.1016/j.apcatb.2019.118043.
[14] Varga T, Vásárhelyi L, Ballai G, Haspel H, Oszkó A, Kukovecz Á, Kónya Z. Noble-metal-free iron nitride/nitrogen-doped graphene composite for the oxygen reduction reaction. ACS Omega 2019;4:130–9. https://doi.org/10.1021/acsomega.8b02646.
[15] Bokach D, ten Hoopen S, Muthuswamy N, Buan MEM, Rønning M. Nitrogen-doped carbon nanofiber catalyst for ORR in PEM fuel cell stack: performance, durability and market application aspects. Int J Hydrogen Energy 2016;41:17616–30. https://doi.org/10.1016/j.ijhydene.2016.07.137.
[16] Ania CO, Seredych M, Rodriguez-Castellon E, Bandosz TJ. New copper/GO based material as an efficient oxygen reduction catalyst in an alkaline medium: the role of unique Cu/rGO architecture. Appl Catal B Environ 2015;163:424–35. https://doi.org/10.1016/j.apcatb.2014.08.022.
[17] Lim D, Kong H, Lim C, Kim N, Shim SE, Baeck SH. Spinel-type $NiCo_2O_4$ with abundant oxygen vacancies as a high-performance catalyst for the oxygen reduction reaction. Int J

Hydrogen Energy 2019;44:23775–83. https://doi.org/10.1016/j.ijhydene.2019.07.091.
[18] Tang Q, Jiang L, Liu J, Wang S, Sun G. Effect of surface manganese valence of manganese oxides on the activity of the oxygen reduction reaction in alkaline media. ACS Catal 2014;4:457–63. https://doi.org/10.1021/cs400938s.
[19] Stoerzinger KA, Risch M, Han B, Shao-Horn Y. Recent insights into manganese oxides in catalyzing oxygen reduction kinetics. ACS Catal 2015;5:6021–31. https://doi.org/10.1021/acscatal.5b01444.
[20] Sun S, Miao H, Xue Y, Wang Q, Li S, Liu Z. Oxygen reduction reaction catalysts of manganese oxide decorated by silver nanoparticles for aluminum-air batteries. Electrochim Acta 2016;214:49–55. https://doi.org/10.1016/j.electacta.2016.07.127.
[21] Wang CC, Yu Z, Wang XT, Lin B. Enhanced electrocatalytic performance of NiOx@MnOx@graphene for oxygen reduction and evolution reactions. Int J Hydrogen Energy 2018;43:18992–9001. https://doi.org/10.1016/j.ijhydene.2018.08.073.
[22] Wu F, Feng B, Li W, Liu H, Mei Y, Hu W. Efficient oxygen reduction electrocatalysis on Mn_3O_4 nanoparticles decorated N-doped carbon with hierarchical porosity and abundant active sites. Int J Hydrogen Energy 2019;44:26387–95. https://doi.org/10.1016/j.ijhydene.2019.08.139.
[23] Wang W, Geng J, Kuai L, Li M, Geng B. Porous Mn_2O_3: a low-cost electrocatalyst for oxygen reduction reaction in alkaline media with comparable activity to Pt/C. Chem - A Eur J 2016;22:9909–13. https://doi.org/10.1002/chem.201602078.
[24] Jones LHP, Milne AA. Birnessite, a new manganese oxide mineral from Aberdeenshire, Scotland. Mineral Mag J Mineral Soc 1956;31:283–8. https://doi.org/10.1180/minmag.1956.031.235.01.
[25] Deibert BJ, Zhang J, Smith PF, Chapman KW, Rangan S, Banerjee D, Tan K, Wang H, Pasquale N, Chen F, Lee KB, Dismukes GC, Chabal YJ, Li J. Surface and structural investigation of a MnOx birnessite-type water oxidation catalyst formed under photocatalytic conditions. Chem - A Eur J 2015;21:14218–28. https://doi.org/10.1002/chem.201501930.
[26] Zhang X, Yu P, Zhang H, Zhang D, Sun X, Ma Y. Rapid hydrothermal synthesis of hierarchical nanostructures assembled from ultrathin birnessite-type MnO2 nanosheets for supercapacitor applications. Electrochim Acta 2013;89:523–9. https://doi.org/10.1016/j.electacta.2012.11.089.
[27] Sun S, Xue Y, Wang Q, Huang H, Miao H, Liu Z. Cerium ion intercalated MnO_2nanospheres with high catalytic activity toward oxygen reduction reaction for aluminum-air batteries. Elsevier Ltd; 2018. https://doi.org/10.1016/j.electacta.2018.01.057.
[28] Sun S, Miao H, Xue Y, Wang Q, Zhang Q, Dong Z, Li S, Huang H, Liu Z. High electrocatalytic activity of silver-doped manganese dioxide toward oxygen reduction reaction in aluminum-air battery. J Electrochem Soc 2017;164:F768–74. https://doi.org/10.1149/2.0541707jes.
[29] Cao YL, Yang HX, Ai XP, Xiao LF. The mechanism of oxygen reduction on MnO2-catalyzed air cathode in alkaline solution. J Electroanal Chem 2003;557:127–34. https://doi.org/10.1016/S0022-0728(03)00355-3.
[30] McKendry IG, Thenuwara AC, Shumlas SL, Peng H, Aulin YV, Chinnam PR, Borguet E, Strongin DR, Zdilla MJ. Systematic doping of cobalt into layered manganese oxide sheets substantially enhances water oxidation catalysis. Inorg Chem 2018;57:557–64. https://doi.org/10.1021/acs.inorgchem.7b01592.
[31] Thenuwara AC, Shumlas SL, Attanayake NH, Aulin YV, McKendry IG, Qiao Q, Zhu Y, Borguet E, Zdilla MJ, Strongin DR. Intercalation of cobalt into the interlayer of birnessite improves oxygen evolution catalysis. ACS Catal 2016;6:7739–43. https://doi.org/10.1021/acscatal.6b01980.
[32] Ríos E, Abarca S, Daccarett P, Nguyen Cong H, Martel D, Marco JF, Gancedo JR, Gautier JL. Electrocatalysis of oxygen reduction on $Cu_xMn_{3-x}O_4$ ($1.0 \leq x \leq 1.4$) spinel particles/polypyrrole composite electrodes. Int J Hydrogen Energy 2008;33:4945–54. https://doi.org/10.1016/j.ijhydene.2008.06.030.
[33] Lambert TN, Davis DJ, Lu W, Limmer SJ, Kotula PG, Thuli A, Hungate M, Ruan G, Jin Z, Tour JM. Graphene-Ni-α-MnO_2 and -Cu-α-MnO_2 nanowire blends as highly active non-precious metal catalysts for the oxygen reduction reaction. Chem Commun 2012;48:7931–3. https://doi.org/10.1039/c2cc32971a.
[34] Davis DJ, Lambert TN, Vigil JA, Rodriguez MA, Brumbach MT, Coker EN, Limmer SJ. Role of Cu-Ion doping in Cu-α-MnO_2 nanowire electrocatalysts for the oxygen reduction reaction. J Phys Chem C 2014;118:17342–50. https://doi.org/10.1021/jp5039865.
[35] Cao L, Zhao Z, Liu Z, Gao W, Dai S, Gha J, Xue W, Sun H, Duan X, Pan X, Mueller T, Huang Y. Differential surface elemental distribution leads to significantly enhanced stability of PtNi-based ORR catalysts. Matter 2019;1:1567–80. https://doi.org/10.1016/j.matt.2019.07.015.
[36] Mosa IM, Biswas S, El-Sawy AM, Botu V, Guild C, Song W, Ramprasad R, Rusling JF, Suib SL. Tunable mesoporous manganese oxide for high performance oxygen reduction and evolution reactions. J Mater Chem A 2016;4:620–31. https://doi.org/10.1039/C5TA07878D.
[37] McKenzie RM. The synthesis of birnessite, cryptomelane, and some other oxides and hydroxides of manganese. Mineral Mag 1971;38:493–502. https://doi.org/10.1180/minmag.1971.038.296.12.
[38] Boumaiza H, Coustel R, Medjahdi G, Ruby C, Bergaoui L. Conditions for the formation of pure birnessite during the oxidation of Mn(II) cations in aqueous alkaline medium. J Solid State Chem 2017;248:18–25. https://doi.org/10.1016/j.jssc.2017.01.014.
[39] Pope CG. X-ray diffraction and the Bragg equation. J Chem Educ 1997;74:129. https://doi.org/10.1021/ed074p129.
[40] Silvester E, Manceau A, Drits VA. Structure of synthetic monoclinic Na-rich birnessite and hexagonal birnessite: II. Results from chemical studies and EXAFS spectroscopy. Am Mineral 1997;82:962–78. https://doi.org/10.2138/am-1997-9-1013.
[41] Wang M, Yagi S. Layered birnessite MnO_2 with enlarged interlayer spacing for fast Mg- ion storage. J Alloys Compd 2019:153135. https://doi.org/10.1016/j.jallcom.2019.153135.
[42] Zhang Q, Luo J, Vileno E, Suib SL. Synthesis of cryptomelane-type manganese oxides by microwave heating. Chem Mater 1997;9:2090–5. https://doi.org/10.1021/cm970129g.
[43] Dias A, Sá RG, Spitale MC, Athayde M, Ciminelli VST. Microwave-hydrothermal synthesis of nanostructured Na-birnessites and phase transformation by arsenic(III) oxidation. Mater Res Bull 2008;43:1528–38. https://doi.org/10.1016/j.materresbull.2007.06.019.
[44] Julien CM, Massot M, Poinsignon C. Lattice vibrations of manganese oxides: Part I. Periodic structures. Spectrochim Acta - Part A Mol Biomol Spectrosc 2004;60:689–700. https://doi.org/10.1016/S1386-1425(03)00279-8.
[45] Thenuwara AC, Shumlas SL, Attanayake NH, Cerkez EB, McKendry IG, Frazer L, Borguet E, Kang Q, Zdilla MJ, Sun J, Strongin DR. Copper-intercalated birnessite as a water oxidation catalyst. Langmuir 2015;31:12807–13. https://doi.org/10.1021/acs.langmuir.5b02936.
[46] Stelmachowski P, Legutko P, Jakubek T, Indyka P, Sojka Z, Holmlid L, Kotarba A. Emission of highly excited electronic

states of potassium from cryptomelane nanorods. Phys Chem Chem Phys 2015;17:26289–94. https://doi.org/10.1039/c5cp04108b.
[47] Wang G, Shao G, Du J, Zhang Y, Ma Z. Effect of doping cobalt on the micro-morphology and electrochemical properties of birnessite MnO_2. Mater Chem Phys 2013;138:108–13. https://doi.org/10.1016/j.matchemphys.2012.11.024.
[48] Fujiwara K, Akedo K, Tasaki Y, Nakatsuka A, Nakayama N. Structure and thermal decomposition of $KxMnO_2 \cdot yH_2O$ prepared by sol-gel method. Trans Mater Res Soc Japan. 2014;34:447–50. https://doi.org/10.14723/tmrsj.34.447.
[49] Cheney MA, Bhowmik PK, Qian S, Joo SW, Hou W, Okoh JM. A new method of synthesizing black birnessite nanoparticles: from Brown to black birnessite with nanostructures. J Nanomater 2008;2008:1–8. https://doi.org/10.1155/2008/763706.
[50] Joo SW, Cheney MA, Bhowmik PK, Moriuchi S, Villalobos M, Qian S. The effect of stirring on the morphology of birnessite nanoparticles. J Nanomater 2008;2008. https://doi.org/10.1155/2008/168716.
[51] Yang LX, Zhu YJ, Cheng GF. Synthesis of well-crystallized birnessite using ethylene glycol as a reducing reagent. Mater Res Bull 2007;42:159–64. https://doi.org/10.1016/j.materresbull.2006.04.038.
[52] Feng Q, Sun E, Yanagisawa K, Yamasaki N. Synthesis of birnessite-type reaction and sodium manganese oxides by solution hydrothermal methods of hydrothermal chemistry. J Ceram Soc Jpn 1997;105:564–8. https://doi.org/10.2109/jcersj.105.564.
[53] Feng Q, Liu L, Yanagisawa K. Effects of synthesis parameters on the formation of birnessite-type manganese oxides. J Mater Sci Lett 2000;19:1567–70. https://doi.org/10.1023/A:1006733308073.
[54] Garrison Sposito. Characterization of particle surface charge. In: Environmetal Particles. Taylor and Francis Group; 2019.
[55] Lyklema. Fundamentals of interface and colloid science, I. London: Academic Press; 1991.
[56] Janusz W, Gałgan A. Electrical double layer at manganese oxides/1:1 electrolyte solution interface. Fizykochem Probl Miner. 2001;35:31–41.
[57] Kosmulski M. Compilation of PZC and IEP of sparingly soluble metal oxides and hydroxides from literature. Adv Colloid Interface Sci 2009;152:14–25. https://doi.org/10.1016/j.cis.2009.08.003.
[58] Xia BY, Yan Y, Li N, Bin Wu H, Lou XWD, Wang X. A metal-organic framework-derived bifunctional oxygen electrocatalyst. Nat Energy. 2016;1:1–8. https://doi.org/10.1038/nenergy.2015.6.
[59] Yadav GG, Gallaway JW, Turney DE, Nyce M, Huang J, Wei X, Banerjee S. Regenerable Cu-intercalated MnO2 layered cathode for highly cyclable energy dense batteries. Nat Commun 2017;8:14424. https://doi.org/10.1038/ncomms14424.
[60] Ambrose J, Barradas RG, Shoesmith DW. Investigations of copper in aqueous alkaline solutions by cyclic voltammetry. J Electroanal Chem 1973;47:47–64. https://doi.org/10.1016/S0022-0728(73)80344-4.
[61] Ratso S, Kruusenberg I, Vikkisk M, Joost U, Shulga E, Kink I, Kallio T, Tammeveski K. Highly active nitrogen-doped few-layer graphene/carbon nanotube composite electrocatalyst for oxygen reduction reaction in alkaline media. Carbon N. Y. 2014;73:361–70. https://doi.org/10.1016/j.carbon.2014.02.076.
[62] Li Y, Kuttiyiel KA, Wu L, Zhu Y, Fujita E, Adzic RR, Sasaki K. Enhancing electrocatalytic performance of bifunctional cobalt–manganese-oxynitride nanocatalysts on graphene. ChemSusChem 2017;10:68–73. https://doi.org/10.1002/cssc.201601188.
[63] Vikkisk M, Kruusenberg I, Ratso S, Joost U, Shulg E, Kink I, Rauwel P, Tammeveski K. Enhanced electrocatalytic activity of nitrogen-doped multi-walled carbon nanotubes towards the oxygen reduction reaction in alkaline media. RSC Adv 2015;5:59495–505. https://doi.org/10.1039/c5ra08818f.
[64] Wang Y, Li Y, Lu Z, Wang W. Improvement of O_2 adsorption for α-MnO_2 as an oxygen reduction catalyst by Zr^{4+} doping. RSC Adv 2018;8:2963–70. https://doi.org/10.1039/c7ra10079e.
[65] Lambert TN, Vigil JA, White SE, Delker CJ, Davis DJ, Kelly M, Brumbach MT, Rodriguez MA, Swartzentruber BS. Understanding the effects of cationic dopants on α-MnO_2 oxygen reduction reaction electrocatalysis. J Phys Chem C 2017;121:2789–97. https://doi.org/10.1021/acs.jpcc.6b11252.
[66] Cheng F, Su Y, Liang J, Tao Z, Chen J. MnO_2-based nanostructures as catalysts for electrochemical oxygen reduction in alkaline media. Chem Mater 2010;22:898–905. https://doi.org/10.1021/cm901698s.
[67] Roche I, Chaînet E, Chatenet M, Vondrák J. Carbon-supported manganese oxide nanoparticles as electrocatalysts for the Oxygen Reduction Reaction (ORR) in alkaline medium: physical characterizations and ORR mechanism. J Phys Chem C 2007;111:1434–43. https://doi.org/10.1021/jp0647986.
[68] Feng J, Liang Y, Wang H, Li Y, Zhang B, Zhou J, Wang J, Regier T, Dai H. Engineering manganese oxide/nanocarbon hybrid materials for oxygen reduction electrocatalysis. Nano Res 2012;5:718–25. https://doi.org/10.1007/s12274-012-0256-8.
[69] Su HY, Gorlin Y, Man IC, Calle-Vallejo F, Norskov JK, Jaramillo TF, Rossmeisl J. Identifying active surface phases for metal oxide electrocatalysts: a study of manganese oxide bi-functional catalysts for oxygen reduction and water oxidation catalysis. Phys Chem Chem Phys 2012;14:14010–22. https://doi.org/10.1039/c2cp40841d.
[70] Lima FHB, Calegaro ML, Ticianelli EA. Investigations of the catalytic properties of manganese oxides for the oxygen reduction reaction in alkaline media. J Electroanal Chem 2006;590:152–60. https://doi.org/10.1016/j.jelechem.2006.02.029.
[71] Peng X, Wang Z, Wang Z, Pan Y. Multivalent manganese oxides with high electrocatalytic activity for oxygen reduction reaction. Front Chem Sci Eng 2018;12:790–7. https://doi.org/10.1007/s11705-018-1706-y.